

# Generation of inner ear sensory epithelia from pluripotent stem cells in 3D culture

Karl R. Koehler<sup>1,2,3</sup>, Andrew M. Mikosz<sup>2,3</sup>, Andrei I. Molosh<sup>2,4</sup>, Dharmeshkumar Patel<sup>2,3</sup> & Eri Hashino<sup>1,2,3</sup>

The inner ear contains sensory epithelia that detect head movements, gravity and sound. It is unclear how to develop these sensory epithelia from pluripotent stem cells, a process that will be critical for modelling inner ear disorders or developing cell-based therapies for profound hearing loss and balance disorders<sup>1,2</sup>. So far, attempts to derive inner ear mechanosensitive hair cells and sensory neurons have resulted in inefficient or incomplete phenotypic conversion of stem cells into inner-ear-like cells<sup>3–7</sup>. A key insight lacking from these previous studies is the importance of the non-neural and preplacodal ectoderm, two critical precursors during inner ear development<sup>8–11</sup>. Here we report the stepwise differentiation of inner ear sensory epithelia from mouse embryonic stem cells (ESCs) in three-dimensional culture<sup>12,13</sup>. We show that by recapitulating *in vivo* development with precise temporal control of signalling pathways, ESC aggregates transform sequentially into non-neural, preplacodal and otic-placode-like epithelia. Notably, in a self-organized process that mimics normal development, vesicles containing prosensory cells emerge from the presumptive otic placodes and give rise to hair cells bearing stereocilia bundles and a kinocilium. Moreover, these stem-cell-derived hair cells exhibit functional properties of native mechanosensitive hair cells and form specialized synapses with sensory neurons that have also arisen from ESCs in the culture. Finally, we demonstrate how these vesicles are structurally and biochemically comparable to developing vestibular end organs. Our data thus establish a new *in vitro* model of inner ear differentiation that can be used to gain deeper insight into inner ear development and disorder.

During neurulation *in vivo*, the definitive ectoderm is subdivided into the neuroectoderm and non-neural ectoderm, the latter of which gives rise to the inner ear (Supplementary Fig. 1a). Recent studies have demonstrated how organogenesis of complex neuroectoderm tissues such as the cerebral cortex and retina can be faithfully reconstituted *in vitro* by culturing ESCs as a floating aggregate in serum-free media (serum-free floating culture of embryoid body-like aggregates with quick reaggregation; SFEBq culture)<sup>12,14,15</sup>. As the inner ear shares a common precursor with these tissues, the definitive ectoderm, we proposed that SFEBq culture could be redirected to generate inner ear epithelia using carefully timed morphogenetic cues (Fig. 1a and Supplementary Fig. 1b). Led by previous studies, we identified a definitive-ectoderm-like epithelium on day 3 of SFEBq culture, before the expression of neuroectoderm-associated proteins on day 5 (Supplementary Fig. 1c–j)<sup>13,16</sup>. During early embryogenesis, activation of bone morphogenetic protein (BMP) signalling is critical for induction of the non-neural ectoderm from the definitive ectoderm epithelium<sup>11,17</sup>. Consistent with this role, in aggregates treated with human BMP4 (hereafter BMP), the non-neural ectoderm marker *Dlx3* was upregulated, whereas the neuroectoderm marker *Sox1* was downregulated (Supplementary Fig. 1k, l). However, BMP-treated aggregates also expressed the mesendoderm marker brachyury (also known as *T*), indicating the undesirable induction of mesoderm or endoderm cell types (Fig. 1b–h and Supplementary Fig. 2b)<sup>18</sup>. To

suppress aberrant mesendoderm induction, we combined BMP treatment with the transforming growth factor- $\beta$  (TGF- $\beta$ ) inhibitor SB-431542 (SB; Fig. 1a)<sup>19</sup>. A combined treatment of SB and BMP (BMP/SB) on day 3 completely abolished brachyury<sup>+</sup> cells in the outer epithelium (Fig. 1d, e, h; see also Supplementary Discussion)<sup>12,18,19</sup>.

To test whether BMP/SB treatment indeed induced non-neural ectoderm, we assessed the cellular composition of BMP/SB-treated aggregates by immunofluorescence at differentiation day 5. Notably, expression of the non-neural ectoderm marker activator protein 2 (AP2, also known as *Tfap2a*) was found predominantly in the E-cadherin (Ecad, also known as *Cdh1*)<sup>+</sup> outer epithelium, but was absent in other regions of treated aggregates (Fig. 1i, j). Moreover, we identified an intermediate layer of

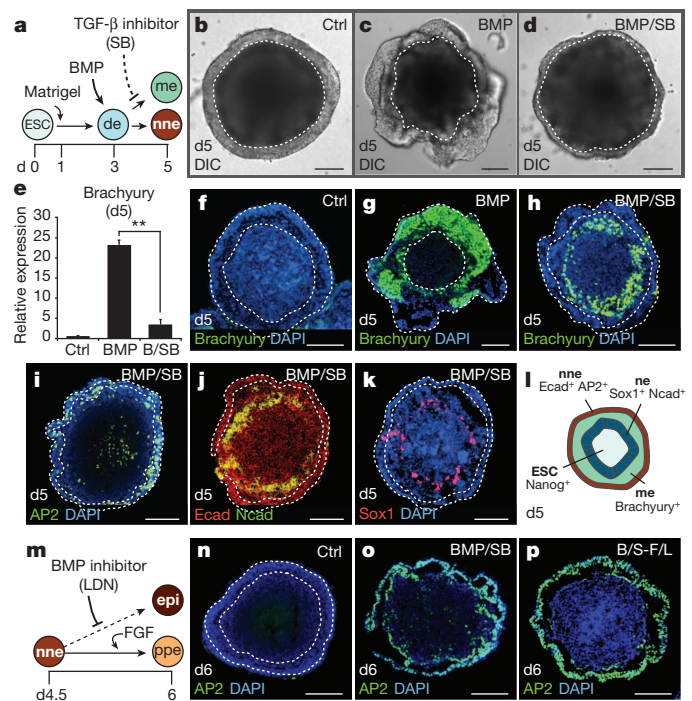


**Figure 1 | Non-neural and preplacodal ectoderm induction in three-dimensional culture.** **a**, Non-neural ectoderm induction strategy. **d**, day; **de**, definitive ectoderm; **me**, mesendoderm; **nne**, non-neural ectoderm. **b–d**, Morphology of control (Ctrl), BMP and BMP/SB aggregates. DIC, differential interference contrast. **e**, SB decreases the level of brachyury expression induced by BMP ( $n = 3$ ;  $**P < 0.01$ ; mean  $\pm$  s.e.m.). **f–h**, Brachyury<sup>+</sup> cells are less prevalent in BMP/SB aggregates. DAPI, 4',6-diamidino-2-phenylindole. **i–k**, BMP/SB aggregates contain an outer AP2<sup>+</sup> Ecad<sup>+</sup> epithelium and an interior Sox1<sup>+</sup> Ncad<sup>+</sup> cell layer. **l**, BMP/SB aggregate composition on day 5. **ne**, neuroectoderm. **m**, Preplacodal ectoderm induction strategy. **epi**, epidermis; **ppe**, preplacodal ectoderm. **n–p**, BMP/SB-FGF/LDN (B/S-F/L) aggregates are distinguished by a thickened AP2<sup>+</sup> epithelium absent in other conditions. Scale bars, 100  $\mu$ m.

<sup>1</sup>Medical Neuroscience Graduate Program, Indiana University School of Medicine, Indianapolis, Indiana 46202, USA. <sup>2</sup>Stark Neurosciences Research Institute, Indiana University School of Medicine, Indianapolis, Indiana 46202, USA. <sup>3</sup>Department of Otolaryngology-Head and Neck Surgery, Indiana University School of Medicine, Indianapolis, Indiana 46202, USA. <sup>4</sup>Department of Psychiatry, Indiana University School of Medicine, Indianapolis, Indiana 46202, USA.

each aggregate with Sox1<sup>+</sup> and N-cadherin (Ncad, also known as Cdh2)<sup>+</sup> cells, indicative of the formation of neuroectoderm (Fig. 1j, k and Supplementary Fig. 1h). In addition, the pluripotency marker Nanog was confined to cells at the core of each aggregate (Supplementary Fig. 2g). Altogether, these data strongly suggest that the outer epithelium of day 5 BMP/SB-treated aggregates represents non-neural ectoderm, which surrounds an interior layer containing a mixture of mesendodermal and neuroectodermal tissues and a central core of pluripotent cells (Fig. 1l and Supplementary Fig. 2). In support of this conclusion, the outer epithelium of BMP/SB samples develops into a Krt5<sup>+</sup> p63 (also known as Trp63)<sup>+</sup> epithelium, mimicking embryonic development of the epidermis (Supplementary Fig. 3).

The preplacodal region, a contiguous band of embryonic head ectoderm, arises from the non-neural ectoderm at the neural tube border and is the precursor to all of the cranial placodes (Supplementary Fig. 4a)<sup>11</sup>. Although BMP signalling is required for induction of non-neural ectoderm, recent studies suggest that subsequent BMP inhibition, along with active fibroblast growth factor (FGF) signalling, is necessary for non-neural cells to select a preplacodal over an epidermal fate (Fig. 1m)<sup>9,20,21</sup>. With this in mind, we began treating BMP/SB aggregates with various combinations of the specific BMP inhibitor LDN-193189 (LDN) and human FGF2. We found that BMP/SB aggregates treated with LDN on day 4.5 maintained expression of *Dlx3*, indicating that BMP inhibition after non-neural induction does not reverse cell fate specification (Supplementary Fig. 4c). Consistent with the preplacodal ectoderm being thickened relative to the surrounding surface

ectoderm<sup>8,11</sup>, we found thickened patches of epithelia in BMP/SB/LDN aggregates that were not present in BMP/SB epithelia (Supplementary Fig. 4b, h). As observed *in vivo*, this morphological change appeared to be dependent on endogenous FGFs, as inhibition of FGF signalling by the small molecule SU5402 abolished epithelial thickening (Supplementary Fig. 5a). A combined treatment of recombinant FGF2 and LDN (hereafter BMP/SB-FGF/LDN) significantly increased the thickness of the epithelium compared to BMP/SB and BMP/SB-LDN aggregates (Fig. 1n–p and Supplementary Fig. 4h). Notably, in >95% of BMP/SB-FGF/LDN aggregates, a thickened Gata3<sup>+</sup> Six1<sup>+</sup> AP2<sup>+</sup> epithelium ruffled and formed ovoid vesicles between days 6 and 8 (Fig. 1p and Supplementary Fig. 4d–j). These and the following data strongly suggest that the outer epithelium of BMP/SB-FGF/LDN-treated aggregates is representative of preplacodal ectoderm.

In vertebrates, the otic placode is derived from a posterior preplacodal region known as the otic-epibranchial placode domain (OEPD; Fig. 2a). The otic placode is demarcated from other developing placodes by expression of the transcription factors Pax2 and Pax8 (see Supplementary Fig. 6 for the *in vivo* situation)<sup>22</sup>. Because the induction of the OEPD requires FGF signalling and the otic placode epithelium thickens, invaginates and forms the otic vesicle<sup>10</sup>, we examined whether the vesicle-forming epithelia of BMP/SB-FGF/LDN aggregates were representative of the primordial inner ear. Our quantitative PCR analysis revealed that Pax2 and Pax8 were significantly upregulated in BMP/SB-FGF/LDN samples compared to other conditions (Fig. 2b, c). By day 6, we observed Pax8<sup>+</sup> cells distributed in placode-like patches throughout the outer Ecad<sup>+</sup> epithelium of BMP/SB-FGF/LDN aggregates only (Fig. 2d, e). Notably, we also observed a population of Pax8<sup>+</sup> Ecad<sup>−</sup> cells in the interior of each aggregate, suggesting formation of mid-hindbrain tissue in this region (Supplementary Fig. 7). The percentage of Pax8<sup>+</sup> Ecad<sup>+</sup> epithelium markedly increased between days 6 and 8 (Fig. 2f, g and Supplementary Fig. 8a–e) and the Pax8<sup>+</sup> Ecad<sup>+</sup> epithelium bore a striking morphological resemblance to the developing otic placode (Supplementary Fig. 6). Of note, we did not observe expression of Pax3 or Pax6 in the outer epithelium, ruling out the development of other cranial placodes (Supplementary Fig. 7c–g). Taken together, these findings show that FGF/LDN treatment is critically important for *in vitro* otic placode induction and that treatment is most effective when performed between days 4 and 5 (Supplementary Fig. 8).

*In vivo*, the prosensory domain of the otic placode/vesicle gives rise to the vestibular/cochlear sensory epithelia and inner ear sensory neurons. Otic prosensory cells are defined by the expression of Pax2, Pax8, Ecad, Sox2 and jagged 1 (Jag1) (Supplementary Figs 6 and 12). On day 8 of differentiation, BMP/SB-FGF/LDN aggregates were transferred to a serum-free floating culture to allow self-guided differentiation. In each aggregate analysed, approximately 24 h after transfer, the interior cell mass breached the outer epithelium and formed a heterogeneous cell layer on the exterior of the aggregate (*n* = 253 aggregates; Fig. 2h, m and Supplementary Fig. 9). This indicated that the outer epithelium transitions to an inner epithelium lining the core of each aggregate. During days 9–12 we observed the continuous evagination of vesicles containing Pax2<sup>+</sup> Ecad<sup>+</sup>, Pax2<sup>+</sup> Pax8<sup>+</sup>, and Sox2<sup>+</sup> Pax8<sup>+</sup> cells from the presumptive OEPD epithelium into the exterior cell layer (Fig. 2h–k and Supplementary Figs 9 and 10), which resulted in ~25 Pax2<sup>+</sup> Pax8<sup>+</sup> Sox2<sup>+</sup> vesicles per aggregate (Fig. 2l). We proposed that endogenous Wnt signalling may underlie induction of vesicles bearing otic prosensory markers in our culture because Wnt signalling is necessary for otic placode formation *in vivo*<sup>10</sup>. Confirming this hypothesis, treatment of aggregates with the Wnt inhibitor XAV939 from days 8–10 significantly decreased the number of prosensory vesicles and, specifically, reduced the prevalence of Pax2<sup>+</sup> vesicles (Fig. 2l). These data indicate that endogenous Wnt signalling induces the formation of otic vesicles from the presumptive otic placode using similar mechanisms as observed *in vivo*. Interestingly, the remaining inner epithelium developed into Krt5<sup>+</sup> p63<sup>+</sup> epidermis and the exterior layer of cells gave rise

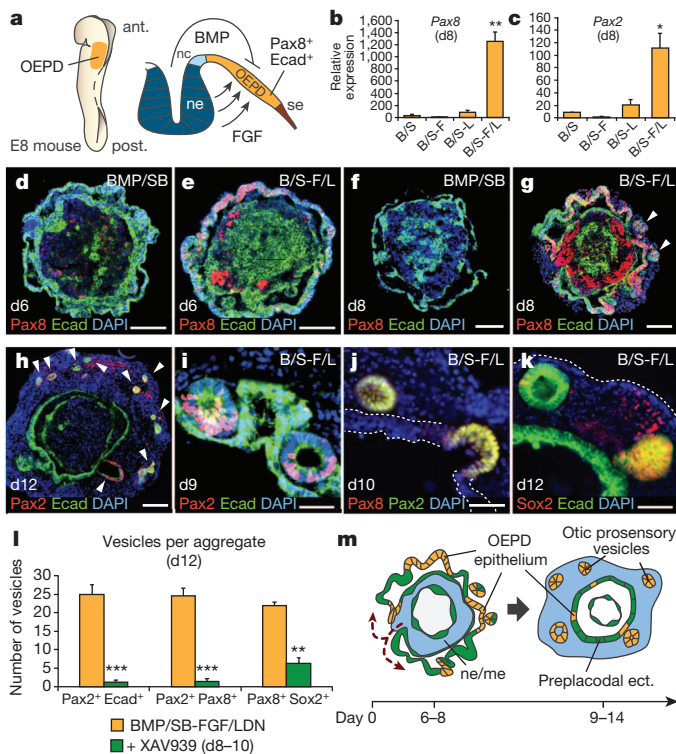


**Figure 2 | Otic induction from the preplacodal epithelium *in vitro*.** **a**, OEPD induction in mice. nc, neural crest; se, surface ectoderm. **b**, **c**, Pax8 (**b**) Pax2 (**c**) messenger RNA expression on day 8 (*n* = 3–4; \**P* < 0.05, \*\**P* < 0.01; mean ± s.e.m.). **d–g**, Pax8 and Ecad expression in BMP/SB aggregates (**d**, **f**) and BMP/SB-FGF/LDN aggregates (**e**, **g**) on days 6 and 8. Arrowheads indicate vesicles. **h**, Day 12 BMP/SB-FGF/LDN aggregate with Pax2<sup>+</sup> Ecad<sup>+</sup> vesicles (arrowheads). **i–k**, Pax2<sup>+</sup> Ecad<sup>+</sup> (**i**), Pax2<sup>+</sup> Pax8<sup>+</sup> (**j**) and Sox2<sup>+</sup> Pax8<sup>+</sup> (**k**) vesicles invaginate from the inner epithelium from days 9–12. **l**, XAV939 decreases the number of vesicles expressing Pax2 and Ecad, Pax2 and Pax8, and Pax8 and Sox2 on day 12. (*n* = 9 aggregates; \*\**P* < 0.01, \*\*\**P* < 0.001; mean ± s.e.m.). **m**, Self-guided, inside-out rearrangement of BMP/SB-FGF/LDN aggregates and formation of otic vesicles. Scale bars, 100 μm (**d–f**, **h**), 50 μm (**i–k**) and 25 μm (**g**).



to mesenchyme-tissue-like cartilage and adipose (Supplementary Fig. 11). The basal ( $p63^+$ ) layer of the inner epithelium was oriented so that the apical surface of the epithelium was facing the interior of the aggregate. Thus, the process of vesicle evagination towards the outside of the aggregate is consistent with the orientation of embryonic otic vesicle invagination into the head mesenchyme (Supplementary Fig. 11).

During development, the prosensory domain of the otic vesicle is destined to become sensory epithelia harbouring  $Myo7a^+$  sensory hair cells. Surprisingly, the epithelia of  $Sox2^+$   $Jag1^+$  vesicles became  $Myo7a^+$  by day 14, mimicking the diffuse  $Myo7a$  staining pattern in the embryonic day (E)9.5 otic vesicle (Fig. 3a, b and Supplementary Fig. 12a–f). By day 16, we found that each aggregate contained  $15.4 \pm 4.8$  ( $n = 12$  aggregates) vesicles lined with  $Myo7a^+$   $Sox2^+$  cells bearing the stereotyped morphology of sensory hair cells with a large nuclei ( $\sim 8\text{-}\mu\text{m}$  diameter) positioned basal to an elongated apical end (Fig. 3c). The  $Myo7a^+$   $Sox2^+$  cells were organized in a radial pattern with the apical end abutting a lumen of varying sizes ( $\sim 5\text{--}1,100\text{-}\mu\text{m}$ -long-axis diameter; Fig. 3c–e). Basal to each layer of  $Myo7a^+$   $Sox2^+$  cells was a tightly arranged layer of  $Sox2^+$  cells reminiscent of supporting cells (Fig. 3c–j and Supplementary Video 1). Mimicking the *in vivo* sensory epithelia, hair cells and supporting cells could be further distinguished by expression of  $Brn3c$  (also known as  $Pou4f3$ ) and cyclin D1, respectively (Supplementary Fig. 13a–f)<sup>23</sup>. F-actin staining revealed tight cell–cell junctions along the luminal surface as well as F-actin<sup>+</sup> espin (Espin)<sup>+</sup> stereocilia bundles (Fig. 3k–o, Supplementary Fig. 13g–i and Supplementary Video 2). Every  $Myo7a^+$  cell analysed also had an acetylated- $\alpha$ -tubulin<sup>+</sup> kinocilium protruding from the

apical end into the lumen (Fig. 3m, n and Supplementary Fig. 13j–m). Stereocilia and kinocilium were not visible at day 16, but the average height increased from day 20 to day 24 and fell within the range of heights recorded from an adult mouse utricle (Fig. 3o)<sup>24</sup>. The hair cells also appeared to be functional on the basis of rapid uptake of FM1-43 dye and the diversity of voltage-dependent currents (Fig. 3p–r and Supplementary Fig. 14)<sup>25,26</sup>. In all cells included in this study we observed outwardly rectifying potassium currents with voltage-dependent activation kinetics to amplitudes ranging from 194 pA to 3,612 pA with a mean of  $1,003 \pm 527$  pA ( $n = 6$ ; Fig. 3r). In addition, some cells were distinguished by the presence of a transient inward current, probably reflecting calcium channel activity (Supplementary Fig. 14k, l). By day 20 each BMP/SB-FGF/LDN aggregate contained  $1,552.3 \pm 83.1$   $Myo7a^+$  cells with typical hair cell morphology, in marked contrast to other conditions that yielded no  $Myo7a^+$  cells ( $\sim 1\text{--}2\%$  of all cells in the aggregate;  $n = 12\text{--}16$  aggregates per condition; Fig. 3s, t). We conclude from these data that the cytoarchitecture, cellular morphology and functional characteristics observed in  $Myo7a^+$   $Sox2^+$  vesicles are identical to sensory epithelia in the inner ear.

There are four distinct populations of hair cells in the mammalian inner ear; type I and type II vestibular and inner and outer cochlear hair cells. We wished to reveal which type of hair cells populated the stem-cell-derived sensory epithelia in our culture. Previous studies have suggested that expression of  $Pax2$  and  $Sox2$  may distinguish vestibular from cochlear hair cells<sup>27,28</sup>. In addition, expression of the calcium-binding protein calbindin 2 ( $Calb2$ ) and  $Sox2$  uniquely label type II vestibular hair cells, whereas calyceal innervation from sensory

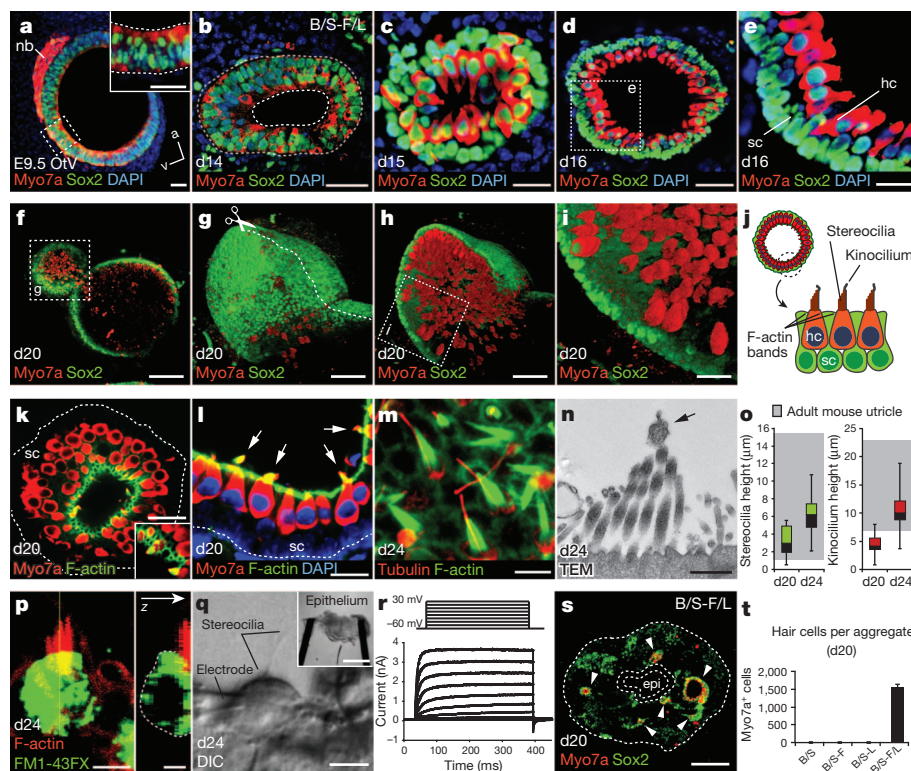


**Figure 3 | Stem-cell-derived otic vesicles generate functional inner ear hair cells.** **a, b**, Expression of  $Myo7a$  in the E9.5 otic vesicle (OtV) (**a**) and day 14 vesicles (**b**). nb, neuroblasts. **c–e**,  $Myo7a^+$   $Sox2^+$  hair cells (hc) with underlying  $Sox2^+$  supporting cells (sc) on days 15 (**c**) and 16 (**d, e**). **f–i**, Whole-mount immunofluorescence for  $Myo7a$  and  $Sox2$  (**f**) and three-dimensional reconstruction (**g–i**) of a vesicle in a day 20 BMP/SB-FGF/LDN aggregate. **j**, Vesicles display the hallmarks of inner ear sensory epithelia. **k–m**, F-actin labels cell–cell junctions on the luminal surface and stereocilia bundles. **m**, Acetylated  $\alpha$ -tubulin (tubulin) labels kinocilium and the cuticular plate. **n**, Transmission electron micrograph (TEM) of stereocilia bundles and kinocilium (arrow). **o**, Distribution of stereocilia and kinocilium heights on

days 20 and 24 compared to adult mouse utricle, with range indicated by grey boxes ( $n > 100$  cells;  $\pm$  max/min). **p**, Representative hair cell following 1-min FM1-43FX incubation, fixation and staining for F-actin. **q**, Representative epithelium preparation (inset) and hair cell during electrophysiological recordings. **r**, Representative voltage–current responses recorded from hair cells. The voltage protocol is shown at the top. **s**, Day 20 aggregate with  $Myo7a^+$   $Sox2^+$  vesicles. Epidermis is indicated by dashed outline. **t**, Number of hair cells on day 20 ( $n = 12\text{--}16$ ; mean  $\pm$  s.e.m.). Scale bars, 250  $\mu\text{m}$  (**f, s, q** (inset)), 50  $\mu\text{m}$  (**d, g, h**), 25  $\mu\text{m}$  (**a–c, e, i, k, l**), 10  $\mu\text{m}$  (**q**), 5  $\mu\text{m}$  (**m, p**) and 250 nm (**n**).

neurons identifies type I vestibular hair cells (Fig. 4a)<sup>27,29,30</sup>. On day 20, nearly all stem-cell-derived hair cells were Sox2<sup>+</sup> Pax2<sup>+</sup> ( $n > 250$  hair cells; Figs 3c–e, i, 4b). Moreover, every hair cell expressed Calb2, suggesting a uniform population of type II vestibular hair cells (Fig. 4c, e). From a structural standpoint, we noted the presence of larger lumen vesicles ( $3.7 \pm 0.3$  per aggregate, defined as  $>50\text{-}\mu\text{m}$ -long-axis diameter,  $n = 15$  aggregates) with regions of sensory (with hair cells) and nonsensory (without hair cells) epithelia identical in organization to a vestibular end organ (Fig. 4d–g and Supplementary Figs 14b, h and 15). Intriguingly, we also observed discrete populations of Calb2<sup>+</sup> and Brn3a<sup>+</sup> Tuj1 (also known as Tubb3)<sup>+</sup> neurofilament (Nefl)<sup>+</sup> neurons extended processes towards the sensory epithelia (Fig. 4h and Supplementary Fig. 16a–d). We were surprised to find that, by day 16, hair cells exhibited punctate expression of ribeye (Ctbp2) colocalized with the postsynaptic and neuronal markers Tuj1, synaptophysin (Syp), Snap25 and Rab3a, indicating the formation of ribbon synapses with adjacent neurons (Fig. 4h–j and Supplementary Fig. 16e–j). Notably, the number of ribbon synapses increased over time in culture, suggesting a maturation process similar to native hair cells in the inner ear (Fig. 4k and Supplementary Fig. 16h–j)<sup>30</sup>. Together, these results indicate that stem-cell-derived vesicles in our culture represent immature vestibular end organs, specifically the utricle and/or saccule<sup>12,23,28</sup>.

In conclusion, our findings highlight a binary mechanism of BMP activation and TGF- $\beta$  inhibition underlying *in vitro* non-neural ectoderm induction. Furthermore, subsequent inhibition of BMP signalling concomitant with activation of FGF signalling are required for preplacodal induction. Notably, the formation of these precursors is

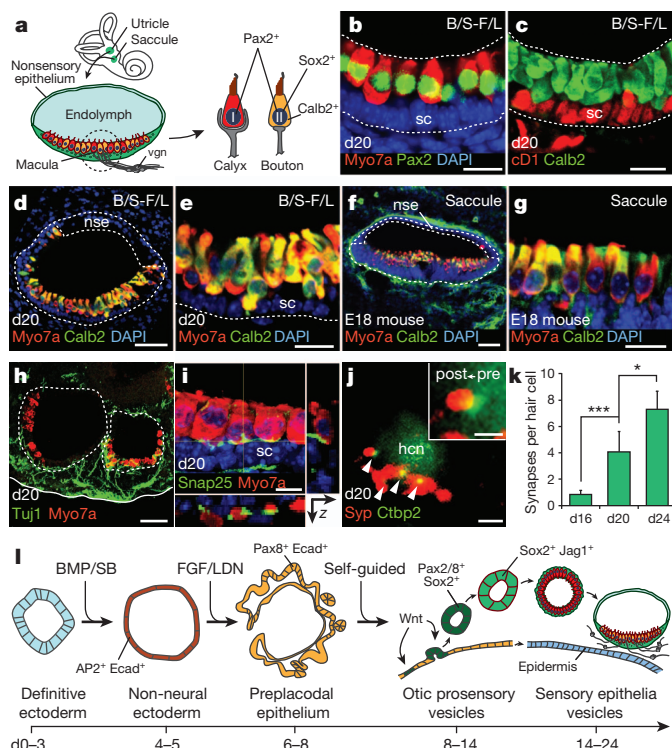


**Figure 4 | Stem-cell-derived sensory epithelia are comparable to immature vestibular end organs.** **a**, Schematic of vestibular end organs and type I/II vestibular hair cells. vgn, vestibular ganglion neurons. **b**, **c**, Pax2 (**b**) and Calb2 (**c**) are expressed in all Myo7a<sup>+</sup> stem-cell-derived hair cells on day 20. CyclinD1 (cD1) is expressed in supporting cells. **d–g**, The structural organization of vesicles with Calb2<sup>+</sup> Myo7a<sup>+</sup> hair cells mimics the E18 mouse saccule (sagittal view) *in vivo*. nse, nonsensory epithelium. **h**, Tuj1<sup>+</sup> neurons extending processes to hair cells. **i**, The synaptic protein Snap25 is localized to the basal end of hair cells. **j**, The postsynaptic marker Syp colocalizes with Ctbp2 (arrowheads and inset). hcn, hair cell nucleus. **k**, Quantification of synapses on day 16, 20 and 24 hair cells ( $n > 100$  cells,  $*P < 0.05$ ,  $***P < 0.001$ ; mean  $\pm$  s.d.). **l**, Overview of *in vitro* differentiation. Scale bars, 50  $\mu\text{m}$  (**d**, **f**, **h**), 25  $\mu\text{m}$  (**b**, **c**, **e**, **g**), 10  $\mu\text{m}$  (**i**), 5  $\mu\text{m}$  (**j**).

sufficient to trigger self-guided induction of the sensory epithelia, from which hair cells with structural and functional properties of native mechanosensitive hair cells in the inner ear spontaneously arise in significant numbers ( $\sim 1,500$  hair cells per aggregate; see Fig. 4l). This new approach can not only be used as a potent model system to elucidate the mechanisms underlying inner ear development, but will also provide an easily accessible and reproducible means of generating hair cells for *in vitro* disease modelling, drug discovery or cellular therapy experiments.

## METHODS SUMMARY

The SFEBq culture system was performed as described previously, but with major modifications<sup>12</sup>. On day 3 of the protocol, BMP4 (10 ng ml<sup>-1</sup>) and SB-431542 (1  $\mu\text{M}$ ) were added to each well at 5 $\times$  concentration in 25  $\mu\text{l}$  of fresh media. On day 4.5, FGF2 (25 ng ml<sup>-1</sup>) and LDN-193189 (100 nM) were added to each well at 6 $\times$  concentration in 25  $\mu\text{l}$  of fresh media.

**Full Methods** and any associated references are available in the online version of the paper.

**Received 18 November 2012; accepted 13 May 2013.**

**Published online 10 July 2013.**

- Bermingham-McDonogh, O. & Reh, T. A. Regulated reprogramming in the regeneration of sensory receptor cells. *Neuron* **71**, 389–405 (2011).
- Brigande, J. V. & Heller, S. *Quo vadis*, hair cell regeneration? *Nature Neurosci.* **12**, 679–685 (2009).
- Ouji, Y., Ishizaka, S., Nakamura-Uchiyama, F. & Yoshikawa, M. *In vitro* differentiation of mouse embryonic stem cells into inner ear hair cell-like cells using stromal cell conditioned medium. *Cell Death Dis.* **3**, e314 (2012).
- Oshima, K. *et al.* Mechanosensitive hair cell-like cells from embryonic and induced pluripotent stem cells. *Cell* **141**, 704–716 (2010).
- Kondo, T. *et al.* Tlx3 exerts context-dependent transcriptional regulation and promotes neuronal differentiation from embryonic stem cells. *Proc. Natl Acad. Sci. USA* **105**, 5780–5785 (2008).
- Reyes, J. H. *et al.* Glutamatergic neuronal differentiation of mouse embryonic stem cells after transient expression of neurogenin 1 and treatment with BDNF and GDNF: *in vitro* and *in vivo* studies. *J. Neurosci.* **28**, 12622–12631 (2008).
- Chen, W. *et al.* Restoration of auditory evoked responses by human ES-cell-derived otic progenitors. *Nature* **490**, 278–282 (2012).
- Schlosser, G. Induction and specification of cranial placodes. *Dev. Biol.* **294**, 303–351 (2006).
- Pieper, M., Ahrens, K., Rink, E., Peter, A. & Schlosser, G. Differential distribution of competence for placodal and neural crest induction to non-neural and neural ectoderm. *Development* **139**, 1175–1187 (2012).
- Groves, A. K. & Fekete, D. M. Shaping sound in space: the regulation of inner ear patterning. *Development* **139**, 245–257 (2012).
- Grocott, T., Tambalo, M. & Streit, A. The peripheral sensory nervous system in the vertebrate head: a gene regulatory perspective. *Dev. Biol.* **370**, 3–23 (2012).
- Eiraku, M. *et al.* Self-organizing optic-cup morphogenesis in three-dimensional culture. *Nature* **472**, 51–56 (2011).
- Suga, H. *et al.* Self-formation of functional adenohypophysis in three-dimensional culture. *Nature* **480**, 57–62 (2011).
- Eiraku, M. *et al.* Self-organized formation of polarized cortical tissues from ESCs and its active manipulation by extrinsic signals. *Cell Stem Cell* **3**, 519–532 (2008).
- Nakano, T. *et al.* Self-formation of optic cups and storable stratified neural retina from human ESCs. *Cell Stem Cell* **10**, 771–785 (2012).
- Kamiya, D. *et al.* Intrinsic transition of embryonic stem-cell differentiation into neural progenitors. *Nature* **470**, 503–509 (2011).
- Wilson, P. A. & Hemmati-Brivanlou, A. Induction of epidermis and inhibition of neural fate by Bmp-4. *Nature* **376**, 331–333 (1995).
- Bernardo, A. S. *et al.* BRACHYURY and CDX2 mediate BMP-induced differentiation of human and mouse pluripotent stem cells into embryonic and extraembryonic lineages. *Cell Stem Cell* **9**, 144–155 (2011).
- Chambers, S. M. *et al.* Highly efficient neural conversion of human ES and iPS cells by dual inhibition of SMAD signaling. *Nature Biotechnol.* **27**, 275–280 (2009).
- Kwon, H.-J., Bhat, N., Sweet, E. M., Cornell, R. A. & Riley, B. B. Identification of early requirements for preplacodal ectoderm and sensory organ development. *PLoS Genet.* **6**, e1001133 (2010).
- Kwon, H.-J. & Riley, B. B. Mesendodermal signals required for otic induction: Bmp-antagonists cooperate with Fgf and can facilitate formation of ectopic otic tissue. *Dev. Dyn.* **238**, 1582–1594 (2009).
- Ladher, R. K., O'Neill, P. & Begbie, J. From shared lineage to distinct functions: the development of the inner ear and epibranchial placodes. *Development* **137**, 1777–1785 (2010).
- Laine, H., Sulg, M., Kirjavainen, A. & Pirvola, U. Cell cycle regulation in the inner ear sensory epithelia: role of cyclin D1 and cyclin-dependent kinase inhibitors. *Dev. Biol.* **337**, 134–146 (2010).
- Li, A., Xue, J. & Peterson, E. H. Architecture of the mouse utricle: macular organization and hair bundle heights. *J. Neurophysiol.* **99**, 718–733 (2008).
- Meyers, J. R. *et al.* Lighting up the senses: FM1-43 loading of sensory cells through nonselective ion channels. *J. Neurosci.* **23**, 4054–4065 (2003).

26. Géléoc, G. S. G., Risner, J. R. & Holt, J. R. Developmental acquisition of voltage-dependent conductances and sensory signaling in hair cells of the embryonic mouse inner ear. *J. Neurosci.* **24**, 11148–11159 (2004).
27. Oesterle, E. C., Campbell, S., Taylor, R. R., Forge, A. & Hume, C. R. Sox2 and Jagged1 expression in normal and drug-damaged adult mouse inner ear. *J. Assoc. Res. Otolaryngol.* **9**, 65–89 (2008).
28. Warchol, M. E. & Richardson, G. P. Expression of the Pax2 transcription factor is associated with vestibular phenotype in the avian inner ear. *Dev. Neurobiol.* **69**, 191–202 (2009).
29. Desai, S. S., Zeh, C. & Lysakowski, A. Comparative morphology of rodent vestibular periphery. I. Saccular and utricular maculae. *J. Neurophysiol.* **93**, 251–266 (2005).
30. Lysakowski, A. *et al.* Molecular microdomains in a sensory terminal, the vestibular calyx ending. *J. Neurosci.* **31**, 10101–10114 (2011).

**Supplementary Information** is available in the online version of the paper.

**Acknowledgements** The authors would like to thank G. Oxford for contributing unpublished data and discussion; E. Beans, G. Kamocka, K. Dunn and C. Miller for technical assistance; P. Dolle, R. Romand, J. Williams, J. Meyer, X. Zhang and

T. Cummins for comments and discussion; E. Tobin, R. Meadows, J. Hamilton, S. Majumdar and G. Wagner for editorial assistance. This work was supported by National Institutes of Health (NIH) grants RC1DC010706, R21DC012617 and R01GM086544. K.R.K. was supported by a Paul and Carole Stark Neurosciences Fellowship and an Indiana Clinical and Translational Science Institute Predoctoral Fellowship (NIH TL1RR025759). A.I.M. was supported by NIH R01MH52619 (awarded to A. Shekhar).

**Author Contributions** K.R.K. conceived and designed the study, performed experiments, analysed data, created the figures and wrote the manuscript. A.M.M. and D.P. performed experiments and analysed data. A.I.M. generated electrophysiological data. E.H. helped to design the study, provided financial support, monitored the experiments and wrote the manuscript. All authors read and approved the final manuscript.

**Author Information** Reprints and permissions information is available at [www.nature.com/reprints](http://www.nature.com/reprints). The authors declare no competing financial interests. Readers are welcome to comment on the online version of the paper. Correspondence and requests for materials should be addressed to E.H. (ehashino@iupui.edu) or K.R.K. (krkoehle@iupui.edu).



## METHODS

**ESC culture.** ESCs derived from blastocyst-stage embryos of R1 mice were maintained in feeder-free conditions using 2i-LIF medium as previously described<sup>31</sup>. In brief, ESCs were maintained on gelatin and used for experimentation until passage 40. N2B27 medium consisted of a 1:1 mixture of Advanced DMEM/F12 and Neurobasal medium (Invitrogen) supplemented with 1 mM GlutaMAX (Invitrogen) and 1 mM penicillin/streptomycin (STEMCELL Technologies). 2i-LIF medium was made by supplementing N2B27 medium with 1,000 U ml<sup>-1</sup> leukaemia inhibitory factor (LIF; Millipore), 3  $\mu$ M CHIR99021 (Stemgent) and 1  $\mu$ M PD0325901 (Santa Cruz).

Days 0–3 of SFEBq differentiation were performed as described with slight modifications<sup>32</sup>. In brief, ESCs were dissociated with 0.25% trypsin-EDTA, resuspended in differentiation medium and plated 100  $\mu$ l per well (3,000 cells) on 96-well low-cell-adhesion U-bottom plates (Lipidure Coat, NOF). Differentiation medium was G-MEM supplemented with 1.5% knockout serum replacement (Invitrogen), 0.1 mM nonessential amino acids, 1 mM sodium pyruvate, 1 mM penicillin/streptomycin and 1 mM 2-mercaptoethanol. On day 1, half of the medium in each well was exchanged for fresh differentiation medium containing Matrigel (2% (v/v) final concentration). On day 3 of the protocol, BMP4 (10 ng ml<sup>-1</sup>) and SB-431542 (1  $\mu$ M) were added to each well at 5 $\times$  concentration in 25  $\mu$ l of fresh media. On days 4–5, FGF2 (25 ng ml<sup>-1</sup>) and LDN-193189 (100 nM) were added to each well at 6 $\times$  concentration in 25  $\mu$ l of fresh media. The concentration of Matrigel was maintained at 2% (v/v) throughout days 1–8. On day 8 of differentiation, cell aggregates were transferred to 24-well plates (Lipidure Coat, NOF; 4–8 aggregates per well) in N2 medium containing 1% (v/v) Matrigel. N2 medium contained Advanced DMEM/F12, 1 $\times$  N2 Supplement, 1 mM penicillin/streptomycin or 50  $\mu$ g ml<sup>-1</sup> Normocin (InvivoGen) and 1 mM GlutaMAX. For some experiments small molecules were added to N2 medium before plating the aggregates. Half of the medium was changed every day during long-term floating culture for up to 30 days.

**Signalling molecules and recombinant proteins.** The following small molecules and recombinant proteins were used: recombinant human BMP4 (10 ng ml<sup>-1</sup>; Stemgent), human FGF2 (25 ng ml<sup>-1</sup>; PeproTech), XAV939 (1  $\mu$ M; Santa Cruz), SU5402 (10  $\mu$ M; BioVision), SB-431542 (1  $\mu$ M; Tocris Bioscience) and LDN-193189 (100 nM; Stemgent). Notably, we have obtained comparable results using concentrations of up to 1  $\mu$ M LDN-193189.

**Quantitative PCR.** As described previously<sup>33</sup>, RNA was isolated using the RNeasy Minikit (Qiagen) and treated with TURBO DNase (Ambion). Single-stranded complementary DNA was synthesized using Omniscript reverse transcriptase (Qiagen) and Oligo-dT primers. All amplicons had standardized sizes of 100–110 base pairs. cDNA samples were amplified on an ABI PRISM 7900HT Sequence Detection System (Applied Biosystems) using the SYBR Green PCR Master Mix (Applied Biosystems). For each PCR reaction, a mixture containing cDNA template (5 ng), Master Mix, and forward and reverse primers (400 nM each) was treated with uracil N-glycosylase at 50 °C for 2 min before undergoing the following program: 1 cycle, 95 °C, 10 min; 45 cycles, 95 °C, 15 s, 60 °C, 1 min; 1 cycle, 95 °C, 15 s, 60 °C, 15 s, 95 °C, 15 s; 72 °C, hold. Melting curve analysis was performed to confirm the authenticity of the PCR product. The mRNA level for each gene was calculated relative to *L27* mRNA expression.

Primers used: *Dlx3* forward: CAGTACGGAGCGTACCGGA, reverse: TGC CGTTACCATGCGAACC; *Sox1* forward: AACGAGATCGGGTCAAG, reverse: ATCTCCGAGTTGTGCATCTT; *brachyury* forward: CACACGGCTGTGAGAG GTACCC, reverse: TGTCCGCATAGTTGGAGAGCTC; *Pax8* forward: CGGCG ATCCCTCACAACCTCG, reverse: TGGGCCAAGTCCACAATGCG; *Pax2* forward: CCGCTGTGACCGGTGCTGATAT, reverse: TGGGTTGCCTGAGAACTCG CTC.

**Immunohistochemistry.** Aggregates were fixed with 4% paraformaldehyde. The fixed specimens were cryoprotected with a graded treatment of 10, 20 and 30% sucrose and then embedded in tissue freezing medium. Frozen tissue blocks were sectioned into 10- or 12- $\mu$ m cryosections. For immunostaining, a 3% goat or horse serum and 0.1% Triton X-100 solution was used for primary antibody incubation. An Alexa Fluor 488-conjugated anti-mouse IgG or anti-rat IgG and an Alexa Fluor 568-conjugated anti-rabbit IgG (Invitrogen) were used as secondary antibodies. A DAPI counterstain was used to visualize cellular nuclei (Vector, VectaShield). For whole-mount staining, aggregates were placed directly into blocking solution with 1% Triton X-100 following fixation. For confocal imaging and three-dimensional reconstruction experiments, following secondary antibody incubation, aggregates were cleared using ScaleA2 solution for 1–2 days followed by ScaleB4 treatment for another 2 days as described previously<sup>34</sup>. Microscopy was performed on a Nikon TE2000 inverted microscope or an Olympus FV1000-MPE confocal/multiphoton microscope. Three-dimensional reconstruction was performed using Voxxx (custom software developed by Indiana Center for Biological Microscopy).

The following antibodies were used: anti-E-cadherin (rabbit, Abcam; mouse, BD Biosciences), anti-N-cadherin (mouse, BD Bioscience), anti-Sox1 (rabbit, Cell Signaling Technologies), anti-Nanog (rabbit, Abcam), anti-brachyury (goat, Santa

Cruz Biotechnology), anti-AP2 $\alpha$  (mouse, DSHB), anti-Pax8 (rabbit, Abcam), anti-Pax2 (rabbit, Invitrogen; mouse, Abnova), anti-Sox2 (mouse, BD Biosciences), anti-Jag1 (rabbit, LSBio), anti-p27<sup>kip1</sup> (mouse, BD Biosciences), anti-myosinVIIa (rabbit, Proteus), anti-acetylated- $\alpha$ -tubulin (mouse, Abcam), anti-Tuj1 (mouse, Covance), anti-Calb2 (mouse, Millipore), anti-Caspr1 (mouse, NeuroMAB), anti-Caspr2 (mouse, NeuroMAB), anti-p63 (mouse, Santa Cruz Biotechnology), anti-cytokeratin 5 (rabbit, Sigma), anti-Nefl (rabbit, Millipore), anti-Brn3a (mouse, Millipore), anti-islet1 (mouse, DSHB), anti-Syp (rabbit, Invitrogen), anti-Brn3c (mouse, Santa Cruz Biotechnology), anti-Ctbp1 and anti-Ctbp2 (mouse, BD Biosciences), anti-Rab3 (mouse, BD Biosciences), anti-Snap25 (mouse, BD Biosciences), anti-Pax6 (rabbit, Abcam), anti-Pax3 (mouse, DSHB), anti-aPKC (rabbit, Santa Cruz Biotechnology), anti-laminin-B1 (rat, Abcam). For most of the antibodies, mouse embryonic tissue sections were used as positive controls. Mouse embryos were dissected from time pregnant CD-1 mice using a protocol approved by the Institutional Animal Care and Use Committee at Indiana University School of Medicine. The embryo fixation and processing procedure was identical to that used for cell aggregates.

The Alcian blue staining procedure was modified from a previously reported method<sup>35</sup>. In brief, cryosections were incubated in Alcian blue staining solution for 10 min and subsequently de-stained using 60% ethanol/40% acetic acid for 20 min. A final eosin stain was performed for 30 s. For Oil Red O staining, cryosections were kept in 60% isopropanol for 2 min and then placed in freshly prepared Oil Red O stain for 5 min followed by a 30-s haematoxylin stain.

**Image analysis.** The percentage of epithelial cells expressing Pax8 and Ecad was established by analysing serial sections of day 6 and day 8 aggregates. Data are representative of 6–8 aggregates from at least 3 separate experiments. For analysis of each aggregate, 5 cryosections were chosen at random positions along the z-axis of the aggregate. Using Nikon Elements or NIH ImageJ software, the Ecad<sup>+</sup> outer epithelium was outlined and cell counting of DAPI and Pax8<sup>+</sup> nuclei along the length of the epithelium established a percentage for each cryosection.

The apparent thickness of epithelia was determined by analysing cryosections stained with Ncad (control) or Ecad (all other conditions) on days 3–6. Data are representative of 6–8 aggregates from at least 3 separate experiments. For each aggregate, 3 serial sections were analysed. Five points along the epithelium were randomly chosen and the thickness was measured using Nikon Elements image analysis tools.

Similarly, the number of Myo7a<sup>+</sup> hair cells in each day 20 aggregate was determined by analysing 10- $\mu$ m serial cryosections. Each biological sample represents the average number of hair cells counted in 4–6 cell aggregates and data are representative of the average from 3 separate experiments (15 aggregates total for each condition). Odd and even numbered cryosections were analysed separately and averaged to avoid double counting. The number of vesicles was quantified similarly, but every third section was analysed to avoid double counting and allow for analysis of 3 separate staining combinations. Vesicles with a long axis diameter larger than 30  $\mu$ m were accounted for to avoid double counting.

Stereocilia heights were determined by measuring the apparent length of F-actin-labelled structures protruding from Myo7a<sup>+</sup> hair cells on day 20 and 24. Likewise, kinocilium heights were determined by measuring the apparent length of acetylated- $\alpha$ -tubulin-labelled protrusions from Myo7a<sup>+</sup> hair cells. Regions of interest were chosen randomly for analysis and >100 cells were analysed across 3–5 separate epithelia for the data shown in Fig. 3.

Synapses were quantified by analysing day 16, 20 and 24 aggregate sections stained for Syp and Ctbp2 using a previously described method<sup>36</sup>. Regions of interest were chosen randomly for analysis and >100 cells were analysed across 4–5 separate epithelia from 3 separate experiments for the data shown in Fig. 3. Confocal z-stacks were taken of Ctbp2-stained hair cells. The maximum-intensity projections were used to count the number of Ctbp2<sup>+</sup> puncta surrounding each hair cell nuclei.

**Statistical analysis.** Statistical significance was determined using a Student's *t*-test for comparison of two groups or a one-way analysis of variance followed by Tukey's post-hoc test for multiple comparisons, unless stated otherwise. All data were analysed using Prism 6 or Microsoft Excel software.

**FM1-43 labelling.** The presence of functional mechanosensitive channels was confirmed using a FM1-43 dye uptake assay similar to previous studies<sup>25,37,38</sup>. Large lumen aggregates (that is, >500- $\mu$ m-long-axis diameter), identified by their translucency and spherical morphology relative to surrounding tissue, were used for these experiments. Aggregates were incubated in DMEM-F12 containing FM1-43FX (5  $\mu$ M; Invitrogen) for 1 min and then washed 3 $\times$  in fresh N2 medium. A faint cellular outline caused by autofluorescence was used to identify potential hair cells in the vesicle wall. In N2 medium, a 0.25- $\mu$ m tungsten needle was used to puncture each vesicle in an area away from the site of potential hair cells. The punctured vesicles were incubated in DMEM-F12 containing FM1-43FX (5  $\mu$ M) for 1 min with gentle rocking and then washed 3 $\times$  in fresh N2 medium. Vesicles

were imaged to confirm dye uptake and immediately fixed with 4% paraformaldehyde. For some experiments, epithelia were fixed and incubated in PBS containing 1% Triton X-100 and phalloidin conjugated to Alexa Fluor 647 (Invitrogen) to confirm the identity of hair cells.

**Electrophysiological recordings.** On day 24 of differentiation, large lumen vesicles ( $>500\text{-}\mu\text{m}$  diameter) were dissected from cell aggregates following a 30-min incubation in DMEM/F12 containing dispase (STEMCELL Technologies). Epithelial regions containing hair cells were identified on the basis of a thickened morphology relative to the rest of the vesicle epithelium. Two incisions were made using tungsten needles on the opposite side of the vesicle in order to expose and flatten the hair-cell-containing epithelium. The flattened epithelium was mounted onto round glass coverslip and held in position by two wires glued to the coverslip using MDX4-4210 (Corning). The coverslip was then placed in a submersion-type slice chamber mounted on the stage of a Nikon E600FN Eclipse microscope. Electrophysiological recordings were performed under continuous perfusion of oxygenated artificial cerebrospinal fluid that contained the following (in mM): 130 NaCl, 3.5 KCl, 1.1  $\text{KH}_2\text{PO}_4$ , 1.3  $\text{MgCl}_2$ , 2.5  $\text{CaCl}_2$ , 30  $\text{NaHCO}_3$ , 10 glucose, pH 7.4 (320 mOsm  $\text{kg}^{-1}$ ). Recording pipettes were pulled from borosilicate capillary glass (WPI) with resistances ranging from 2 to 3 M $\Omega$ . Recording pipettes were filled with a potassium gluconate-based recording solution that contained the following (in mM): 130 K-gluconate, 3 KCl, 3  $\text{MgCl}_2$ , 5 phosphocreatine, 2 K-ATP, 0.2 NaGTP, 10 HEPES, pH 7.3 (290 mOsm  $\text{kg}^{-1}$ ). Whole-cell access resistances were monitored throughout each experiment and ranged from 5–20 M $\Omega$ ; a change of 15% was deemed acceptable.

Hair cells were identified with a 40 $\times$  water-immersion objective and differential interference contrast. Only cells with hair bundles on their apical surface were chosen for recording. Positive pressure was maintained as the recording pipette was lowered into the epithelium. When the recording pipette touched the membrane, positive pressure was released and tight seal was formed. Recordings were obtained at 30  $^{\circ}\text{C}$  using solution inline heater (Warner Instruments). The cells were held at  $-60\text{ mV}$ , and data were acquired using whole-cell technique in voltage-clamp mode using a Multiclamp 700B amplifier (Molecular Devices) coupled to a Digidata 1332A board (Molecular Devices). The data were analysed using the pClamp 10.2 (Molecular Devices). All chemicals were purchased from Sigma-Aldrich.

**Transmission electron microscopy.** Day 24 aggregates were fixed in 2% paraformaldehyde/2% glutaraldehyde in 0.1 M phosphate buffer. After fixation the

specimens were rinsed with phosphate buffered saline followed by post-fixation with 1% osmium tetroxide. Thereafter, the aggregates were dehydrated through a series of graded ethyl alcohols and embedded in Embed 812 (Electron Microscopy Sciences). Ultra-thin sections (70–80 nm) were cut, stained with uranyl acetate and viewed on a Tecnai BioTwin (FEI) transmission electron microscope at 80 kV. Digital images were taken with an Advanced Microscope Techniques couple-charged device camera.

**Western blot analysis.** Cell aggregates were lysed in radioimmunoprecipitation assay buffer supplemented with a protease inhibitor cocktail (Roche). Cell extracts were centrifuged at 13,000 r.p.m., 4  $^{\circ}\text{C}$  for 10 min to remove insoluble debris and chromosomal DNA. Proteins were separated by denaturing SDS-PAGE and transferred to PVDF membranes (Biorad). After blocking, membranes were incubated with a primary antibody overnight at 4  $^{\circ}\text{C}$ . An anti- $\beta$ -actin (Sigma) antibody was used for confirmation of equal loading of the samples. Blots were detected with an horseradish peroxidase-conjugated goat anti-rabbit or rabbit anti-mouse antibody (Invitrogen) and visualized with the SuperSignal West Pico or -Femto chemiluminescent detection system (Pierce) and exposed to X-ray film.

31. Ying, Q.-L. *et al.* The ground state of embryonic stem cell self-renewal. *Nature* **453**, 519–523 (2008).
32. Eiraku, M. & Sasai, Y. Mouse embryonic stem cell culture for generation of three-dimensional retinal and cortical tissues. *Nature Protocols* **7**, 69–79 (2012).
33. Koehler, K. R. *et al.* Extended passaging increases the efficiency of neural differentiation from induced pluripotent stem cells. *BMC Neurosci.* **12**, 82 (2011).
34. Hama, H. *et al.* Scale: a chemical approach for fluorescence imaging and reconstruction of transparent mouse brain. *Nature Neurosci.* **14**, 1481–1488 (2011).
35. Jegalian, B. G. & De Robertis, E. M. Homeotic transformations in the mouse induced by overexpression of a human *Hox3.3* transgene. *Cell* **71**, 901–910 (1992).
36. Coate, T. M. *et al.* Otic mesenchyme cells regulate spiral ganglion axon fasciculation through a Pou3f4/EphA4 signaling pathway. *Neuron* **73**, 49–63 (2012).
37. Gale, J. E., Marcotti, W., Kennedy, H. J., Kros, C. J. & Richardson, G. P. FM1-43 dye behaves as a permeant blocker of the hair-cell mechanotransducer channel. *J. Neurosci.* **21**, 7013–7025 (2001).
38. Hu, Z. & Corwin, J. T. Inner ear hair cells produced in vitro by a mesenchymal-to-epithelial transition. *Proc. Natl Acad. Sci.* **104**, 16675–16680 (2007).